

Nanosized transition metals in controlled environments of phyllosilicate–mesoporous silica composites as highly thermostable and active catalysts†

Cite this: DOI: 10.1039/c3cc43197e

Received 30th April 2013,
Accepted 28th June 2013

DOI: 10.1039/c3cc43197e

www.rsc.org/chemcomm

Carmen Ciotonea,^{ab} Brindusa Dragoi,^a Adrian Ungureanu,^{*a} Alexandru Chiriac,^a Sabine Petit,^b Sébastien Royer^{*b} and Emil Dumitriu^a

Stabilization of transition metals in nano-phyllosilicate phases generated by digestion of mesoporous silica is reported as an efficient route for the formation of highly dispersed metallic nanoparticles with outstanding catalytic activity.

Highly dispersed supported metal (oxide) nanoparticles (NPs) have attracted much interest in the last decade because of their excellent activity and/or selectivity in important oxidation and (de)hydrogenation reactions underpinning most of the catalytic applications in environmental pollution control, energy and fine chemistry.^{1–3} The outstanding catalytic performances of the supported NPs are related to their morphostructural properties (*i.e.*, size and shape),⁴ dispersion (*i.e.*, surface-to-volume ratio and number of defect sites, steps, edges...),⁵ concentration and electronic properties of the metals.⁶ Nevertheless, the low stability of NPs upon high-temperature treatments required for catalyst activation or high-temperature catalytic reactions largely limits their practical applications. Particle sintering and restructuring^{4,5} directly impact catalytic activity, especially when silica is used as a support. Therefore, the design and development of supported metal (oxide) NPs with high and thermally stable dispersion represent ongoing and challenging research tasks. A valuable approach, presented here for the first time, to ensure both dispersion and stability of transition metal (TM) NPs consists of the stabilization of the NPs in controlled environments of phyllosilicate (PS)–mesoporous silica composites. The ordered mesostructured materials have been chosen to have an accurate control over the local environment in which the NPs will be sequentially stabilized. Particularly interesting for our approach are the large-pore mesoporous silica materials with SBA-15 topology, prepared using non-ionic amphiphilic poloxamers as supramolecular templates,⁷ due to several advantages:⁸ (i) high surface areas, well defined pore structures and thick pore walls; (ii) multiple inorganic

species can be simultaneously/sequentially incorporated to yield multi-functional properties; (iii) capability to functionalize their surface by various inorganic or organic components which induce specific local environments for nucleating and growing metal NPs and (iv) versatility of the synthetic procedures to provide an enhanced control over the types of guest inorganic species and, more importantly, their distributions within the micro-mesostructured hosts. In this work, copper, nickel and cobalt phyllosilicate-SBA-15 mesoporous silica composites were proposed to generate highly dispersed and thermally stable metallic active phases. The potential of these materials for heterogeneous catalysis was evaluated for the hydrogenation of cinnamaldehyde as test reaction to characterize the accessibility and dispersion of supported transition metals. PS-derived materials obtained by the deposition precipitation (DP) route were compared with materials prepared by classical wet impregnation (WI) and incipient wetness impregnation (IWI), respectively. The versatility of the approach was demonstrated for catalytic systems based on different TMs such as cobalt (Co_DP), nickel (Ni_DP) and copper (Cu_DP). The materials were characterized in oxidized and reduced forms of transition metals. The experimental details for synthesis and physico-chemical characterization of solids are given in the ESI† file.

Differences between the materials are directly observed by XRD. The patterns recorded for Co_WI and Co_IWI materials (Fig. 1(A)) evidenced the formation of the crystalline Co₃O₄ phase (ICDD 42-1467) with average crystallite sizes of 13.1 and 12.6 nm, respectively, as calculated using the Scherrer equation. Only weak and broad reflections of the highly dispersed Co-PS phase (ICDD 21-0871) are observed at 2θ of $\sim 35^\circ$ and 60° in the XRD pattern of the Co_DP sample.⁹ Similar observation can be made for the Ni- and Cu-containing materials. Thus, NiO and CuO phases are formed by IWI, whereas only PS phases are obtained for DP preparation (Fig. S1, ESI†).

In line with the XRD results, major differences between materials can also be observed in the (HR)TEM images. Thus, Co_WI shows NPs of calibrated size, *i.e.* close to the pore size of the support and confined in the mesopores (Fig. 2(a)). These elementary particles grow in the form of large aggregates separated by silica walls (Fig. 2(a), inset). Mesopore-confined NPs are also observed for Co_IWI without the formation of large aggregates. In this case the aggregates are limited to few particles, as shown in the inset of

^a Technical University 'Gheorghe Asachi' of Iasi, Faculty of Chemical Engineering and Environmental Protection, 73 D. Mangeron Bvd., 700050 Iasi, Romania. E-mail: aungureanu@tuiasi.ro; Tel: +40 232 278683

^b Université de Poitiers, UMR 7285 CNRS, IC2MP, 4 Rue Michel Brunet, Poitiers, 86022 Poitiers Cedex, France. E-mail: sebastien.royer@univ-poitiers.fr; Fax: +33 549453479

† Electronic supplementary information (ESI) available: Materials and methods; characterization results. See DOI: 10.1039/c3cc43197e

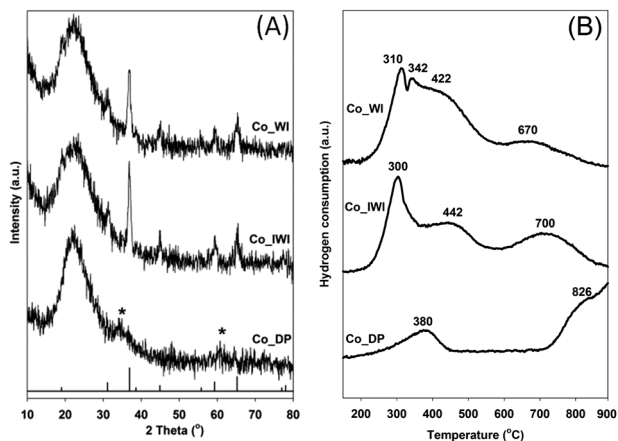


Fig. 1 (A) XRD patterns recorded for Co-containing materials calcined at 500 °C. Bottom: ICDD 42-1467 (Co_3O_4); *: ICDD 21-0871 ($\text{Co}_3(\text{Si}_2\text{O}_5)_2(\text{OH})_2$). (B) TPR profiles of cobalt-containing materials.

Fig. 2(b). In contrast, the Co_DP sample shows completely different morphostructural properties: (i) alteration of the mesopore long-range ordering; (ii) absence of mesopore-confined Co_3O_4 NPs; (iii) appearance of highly dispersed filamentous particles (Fig. 2(c)). Exactly similar observations can be made for Ni_DP (Fig. 2(d)) and Cu_DP (Fig. S4, ESI[†]). This filamentous morphology is characteristic of metal phyllosilicates^{10,11} and confirms that the DP route leads to the stabilization of TMs in the phyllosilicate phases.

The nitrogen adsorption–desorption isotherms of the materials are shown in Fig. S2 (ESI[†]) and the corresponding textural properties are gathered in Table 1. Co_WI and Co_IWI samples exhibit IUPAC type IV isotherms with H1 hysteresis loops, which are typical for mesoporous materials with cylindrical pores, and usually obtained for ordered SBA-15 materials.¹² As compared with the parent SBA-15, the values of surface areas and pore volumes are found to decrease for the samples obtained by impregnation. Also, the decrease in micropore surface area and volume suggests partial plugging of intrawall micropores by oxide clusters which are confined in the primary mesopores of the SBA-15

Table 1 Textural properties of derived TM-containing materials

Sample	M/wt%	$S_{\text{BET}}/\text{m}^2 \text{g}^{-1}$	$S_{\mu}/\text{m}^2 \text{g}^{-1}$	$V_{\text{p}}/\text{cm}^3 \text{g}^{-1}$	$V_{\mu}/\text{cm}^3 \text{g}^{-1}$	D_{p}/nm
SBA-15	—	729	139	1.28	0.061	9
Co_WI	4.5	516	59	0.98	0.023	9
Co_IWI	5.1	476	47	0.89	0.017	9
Co_DP	5.1	363	5	1.11	0.001	11
Ni_DP	4.4	354	33	1.20	0.011	11
Cu_DP	6.1	327	28	1.09	0.012	12

M, metal loading by ICP; S_{BET} and S_{μ} , total and micropore surface area; V_{p} and V_{μ} , total and micropore volume; D_{p} , mean mesopore size.

host (Fig. 2).¹³ For Co_DP, the synthesis conditions (slightly alkaline pH) induced modification of the SBA-15 pore network architecture, originating from silica digestion necessary for phyllosilicate crystallisation, and consequently the surface area decreased two times (Table 1). Likewise, the isotherms show less defined hysteresis loops which are shifted to higher P/P_0 values, as compared with SBA-15. This indicates a broader pore size distribution as well as larger mesopores. An increase in mesopore size as well as change in mesopore shape are obvious in the TEM images, where large pores (>10 nm) are observed (Fig. 2(c)). Similar results were obtained for Ni_DP and Cu_DP, with loss of surface area and an increase in pore size because of the partial shrinkage of SBA-15 mesostructure. However, while Co_DP presents very limited microporosity, the two other materials present significant fraction of micropores, suggesting that the disappearance of the micropores for Co_DP is due to their transformation into mesopores.⁹

The reducibility of the calcined materials was monitored by TPR (Fig. 1(B) and Fig. S3, ESI[†]), while the crystal phase evolution during TPR was followed by *in situ* XRD. The TPR profiles recorded for Co_WI and Co_IWI (Fig. 1(B)) exhibit three distinct reduction stages: (i) <350 °C, reduction of large Co_3O_4 particles, according to a two-step process ($\text{Co}^{3+} \rightarrow \text{Co}^{2+} \rightarrow \text{Co}^0$);¹⁴ (ii) 420–450 °C, reduction of small Co_3O_4 particles, in interaction with the support; (iii) >600 °C, reduction of cobalt in strong interaction with the support or in the PS phase.¹⁴ These reduction steps were further validated by *in situ* XRD. Thus, the Co_3O_4 phase still observed after reduction at 300 °C

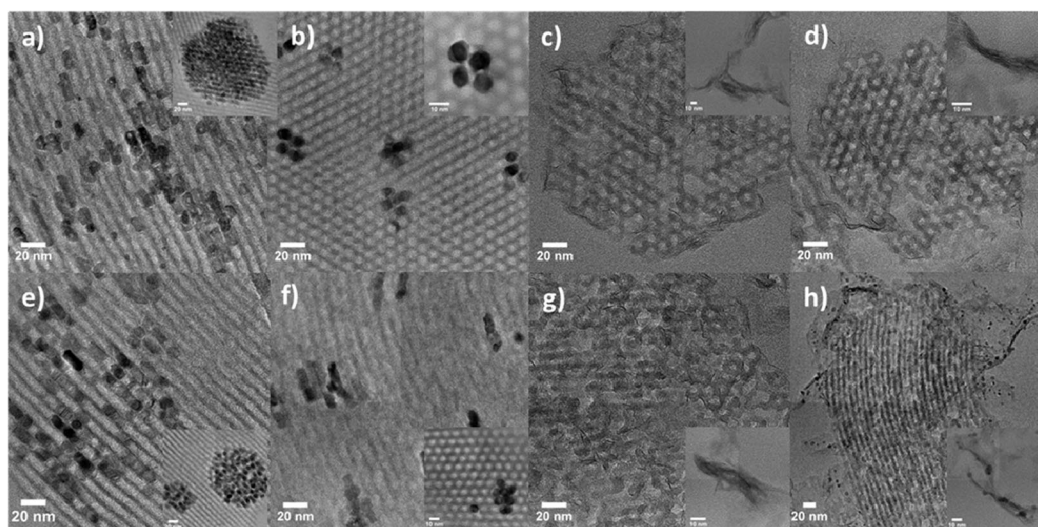


Fig. 2 Representative TEM images recorded for: Co_WI oxidized (a) and reduced (e); Co_IWI oxidized (b) and reduced (f); Co_DP oxidized (c) and reduced (g), and Ni_DP oxidized (d) and reduced (h).

completely disappears at 500 °C along with the appearance of characteristic reflections of the Co⁰ phase (Fig. S5, ESI[†]). Co_DP shows a completely different reduction profile (Fig. 1(B)), with a depressed reduction at low temperature, and main reduction occurring at $T > 750$ °C (incomplete at 900 °C). Such high reduction temperature is unambiguously attributed to the reduction of Co²⁺ in the PS phase,^{9,14,15} in agreement with *vide supra* XRD and TEM results. *In situ* XRD patterns recorded for the Co_DP sample show weak diffraction peaks assigned to the PS phase, highly thermostable and not reducible even after treatment under hydrogen at 500 °C. Albeit a fraction of cobalt oxide was observed to be reduced below 500 °C (Fig. 1(B)), no reflection ascribed to Co⁰ can be detected by XRD. For Cu_DP, Cu²⁺ reduction was observed to occur at 295 °C, indicating the reduction of dispersed particles in strong interactions with the support.¹⁶ The weak reflections corresponding to the PS phase observed below 300 °C by *in situ* XRD disappeared (Fig. S6, ESI[†]), while Cu⁰ appeared at temperatures higher than 300 °C. However, the intensity and FWHM of Cu⁰ reflection peaks indicate no subsequent sintering of the metallic phase up to 500 °C. Finally, Ni_DP presents a reduction maximum at 664 °C (Fig. S3, ESI[†]), in agreement with the reduction of Ni²⁺ in PS phases (1:1 PS, ~550 °C; 2:1 PS, ~650 °C).^{10,11} For the Ni_DP sample, *in situ* XRD results confirm the stability of the PS phase up to 500 °C, with no sintering of the Ni⁰ phase.

Complementary TEM analysis was performed to evaluate the dispersion of the metallic phase (Fig. 2). Fibrous Co-PS particles are always observed for Co_DP samples after reduction at 500 °C (Fig. 2(g)). Very small metallic NPs were also observed, issued from partial reduction of TM cations in the PS phase. However, no large metallic particles can be observed throughout the analyzed grains, confirming the limited sintering of NPs in this material. In contrast, large metallic aggregates of ~10 nm in size appeared for Co_WI and Co_IWI (Fig. 2(e and f)). The reduction of the Ni_DP sample (Fig. 2(h)) leads to the formation of fine and dispersed metallic NPs, even if filamentous particles are still observed. Due to the lower thermal stability of the 1:1 PS phase compared with 2:1 PS,^{11,17} Ni⁰ NPs could originate from the reduction of the 1:1 PS phase, while the reminiscent filamentous phase may correspond to the 2:1 PS phase. The small size of the generated NPs can explain the absence of Ni⁰ reflection in the corresponding XRD pattern (Fig. S5, ESI[†]). Finally, similar morphology

is obtained for Cu_DP (Fig. S4, ESI[†]), TEM images displaying only traces of filamentous particles besides highly dispersed Cu⁰ NPs. Again, the limited size of the generated metallic NPs could be at the origin of the weak and broad reflections observed in Fig. S5 (ESI[†]).

Catalytic activity evolutions (hydrogenation of cinnamaldehyde, Scheme S1, ESI[†]) highlight the important benefit obtained over the DP-materials compared with the WI and IWI derived materials (Fig. 3, catalytic data gathered in Table S1, ESI[†]). Thus, a 2.5-fold higher initial activity is calculated for Co_DP as compared with Co_WI and Co_IWI, despite the incomplete reduction of cobalt under the selected conditions. This result evidenced the remarkable benefit in the accessibility of metallic sites over DP-derived materials. Ni- and Cu-containing DP-materials were also compared with their homologues obtained by the IWI route (Fig. 3), confirming the outstanding activity of the DP-materials. Nevertheless, the chemoselectivity was not significantly affected by the preparation route. The small differences in selectivity (Table S1, ESI[†]) can be related to the modification of adsorption site density with metal particle size. For example, large particles are favourable to the CNA adsorption *via* C=O bonds due to a higher proportion of dense Co(111) faces,¹⁸ which can explain the slightly higher selectivity to CNOL obtained for Co_WI and Co_IWI catalysts.

The stabilization of TM in a highly dispersed state in the PS phase is hence evidenced as a powerful route to produce highly active metallic catalysts. The strong metal-support interactions result in limited particle sintering during reduction, given highly dispersed metallic NPs. Due to the small size of NPs, catalytic activity is remarkably enhanced for PS-mediated metallic catalysts.

This work was partially supported by two grants of the Romanian National Authority for Scientific Research, CNCS – UEFISCDI (project numbers PN-II-ID-PCE-2011-3-0868 and PN-II-RU-TE-2012-3-0403).

Notes and references

- J. M. Campelo, D. Luna, R. Luque, J. M. Marinas and A. A. Romero, *ChemSusChem*, 2009, **2**, 18.
- H. L. Jiang and Q. J. Xu, *Chem. Mater.*, 2011, **21**, 13705.
- J. Greeley and J. Mavrikakis, *Nat. Mater.*, 2004, **3**, 810.
- J. R. A. Sietsma, J. D. Meeldijk, M. Versluijs-Helder, A. Broersma, A. J. van Dillen, P. E. de Jongh and K. P. de Jong, *Chem. Mater.*, 2008, **20**, 2921.
- P. Munnik, M. Wolters, A. Gabriëlsson, S. D. Pollington, G. Headdock, J. H. Bitter, P. E. de Jongh and K. P. J. de Jong, *J. Phys. Chem. C*, 2011, **115**, 14698.
- D. Duprez, M. Demicheli, P. Marecot, J. Barbier, O. A. Feretti and E. N. J. Ponzi, *J. Catal.*, 1990, **124**, 324.
- G. J. de, A. A. Soler-Illia, E. L. Crepaldi, D. Grosso and C. Sanchez, *Curr. Opin. Colloid Interface Sci.*, 2003, **8**, 109.
- G. L. Athens, R. M. Shayib and B. F. Chmelka, *Curr. Opin. Colloid Interface Sci.*, 2009, **14**, 281.
- T. Vrålstad, H. K. Magnusson and J. Sjöblom, *Microporous Mesoporous Mater.*, 2007, **106**, 155.
- P. Burattin, M. Che and C. Louis, *J. Phys. Chem. B*, 1997, **101**, 7060.
- R. Gomez-Reynoso, J. Ramirez, R. Nares, R. Luna and F. Murrieta, *Catal. Today*, 2005, **107–108**, 926.
- D. Zhao, J. Feng, Q. Huo, N. Melosh, G. H. Fredrickson, B. F. Chmelka and G. D. Stucky, *Science*, 1998, **279**, 548.
- A. Ungureanu, B. Dragoi, A. Chiriac, S. Royer, D. Duprez and E. Dumitriu, *J. Mater. Chem.*, 2011, **21**, 12529.
- E. van Steen, G. S. Sewell, R. A. Makhothe, C. Micklethwaite, H. Manstein, M. de Lange and C. T. O'Connor, *J. Catal.*, 1996, **162**, 220.
- G. L. Bezemer, P. B. Radstake, V. Koot, A. J. van Dillen, J. W. Geus and K. P. de Jong, *J. Catal.*, 2006, **237**, 291.
- Z. Huang, F. Cui, J. Xue, J. Zuo, J. Chen and C. Xia, *Catal. Today*, 2012, **183**, 42.
- M. V. Sivaiah, S. Petit, M. F. Beaufort, D. Eyidi, J. Barrault, C. Batiot-Dupeyrat and S. Valange, *Microporous Mesoporous Mater.*, 2011, **140**, 69.
- Y. Nitta, K. Ueno and T. Imantka, *Appl. Catal.*, 1989, **56**, 9.

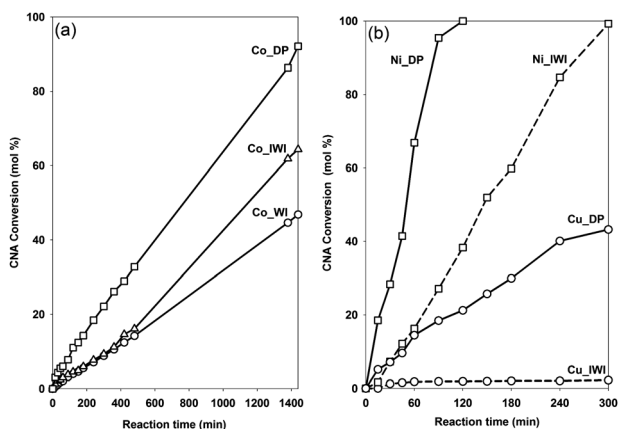


Fig. 3 Catalytic activity in cinnamaldehyde hydrogenation measured for: (a) Co-containing materials; (b) Cu- and Ni-containing materials.